perimentally [23], which should be kept in mind when comparing synthetic and experimental reflection data.

4.5   Wavenumber Integration

Integral transform techniques such as wavenumber integration is an important modeling tool in all disciplines dealing with wave propagation in plane stratified media, such as crustal and exploration seismology, electromagnetics, and of course underwater acoustics.

To determine the acoustic or seismic field parameters at a particular receiver range r and depth z, we must numerically evaluate the inverse Hankel transform of the solution to the depth-separated wave equation at depth z,

$$g(r, z) = \int_0^\infty g(k_r, z) \, J_m(k_r r) \, k_r \, dk_r \,, \qquad (4.93)$$

where $g(r, z)$ represents the field parameter of interest, e.g., acoustic pressure, or a particular displacement or stress component; $g(k_r, z)$ is the associated wavenumber kernel. The order of the Bessel function is $m = 0$, except for the horizontal displacement and shear stress, Eqs. (4.36) and (4.39), where $m = 1$. The numerical evaluation of this integral is complicated by the following features, which must be considered when choosing an integration technique:

- The *infinite* integration interval.
- The *wavenumber discretization* giving rise to *aliasing* and *wrap-around* problems because of the oscillatory nature of the Bessel function, and the variation of the kernel $g(k_r, z)$ which for waveguide problems has poles on or close to the real wavenumber axis.

While the issues associated with the solution of the depth-separated wave equation, e.g. in regard to numerical stability, and therefore the solution techniques, are universal, the evaluation of the wavenumber integral in general is performed differently, depending on the application and the underlying physics. Thus, for example, exploration and crustal seismology are typically dealing with predominantly steep propagation angles because of the relatively short horizontal distance between the sources and a horizontal receiver array on the surface or in the water column, or a vertical borehole array, making the vertical and horizontal propagation scale of the same order of magnitude. Consequently, the response is dominated by discrete arrivals from individual interfaces, with the reflectivity being the property of interest for the environmental characterization. Consequently modal propagation is in general insignificant and is often ignored in the modeling, e.g. by removing the surface of the ocean. In the absence

of modal singularities only the relatively smooth *continuous spectrum* remains, being less susceptible to discretization problems. Further, with the field required at only a few receivers, the integration, and the associated sampling of the kernel, and therefore the solution of the depth-separated wave equation, be performed individually, with the accuracy managed by traditional *convergence analysis* by uniform sampling refinement, or by modern *adaptive integration* techniques, described later.

In contrast, the traditional application of modeling in underwater acoustics has been aimed at predicting the transmission loss over very large horizontal distances, typically 2-3 orders of magnitude larger than the vertical scales of the ocean and the seabed. Consequently, the shallow, subcritical propagation angles are dominating, with a modal propagation pattern dominating beyond typically 10 water depths. Therefore the underwater acoustics propagation is a true *waveguide* problem with dominance of the *discrete spectrum*, and the *continuous spectrum* only being significant at very low frequency and short ranges. In addition, for passive sonar applications the transmission loss is needed for the entire range interval, and the number of receivers is therefore in general very large. For computational reasons the sampling of the wavenumber kernels, and therefore the solution of the depth equations, have been performed on a common frequency-wavenumber grid for all receivers. As a consequence, the accuracy must be ensured more generically than in the seismic problem.

In modern underwater acoustics the role of transmission loss remains important, but new signal processing techniques such as Matched Field Processing, described in Section 10.4-5 require the availability of efficient models providing field estimates on discrete horizontal or vertical arrays, including both magnitude and phase. Also, for active sonar systems modern computer technology has made possible the full time-domain simulation of target scattering and reverberation for specific sonar geometries. Therefore, the integration techniques applied to the similar seismic problems have been adapted to the underwater acoustic modeling frameworks.

In the following we will first described the classical FFT-based integration schemes allowing for very efficient evaluation of the acoustic field at a large number of receiver ranges. The FFT technique is also well suited to illustrate the *discretization problem* because of the direct analogy to periodic solution to cylindrical problems. Then the more direct numerical integrations schemes, based on either fixed or adaptively determined wavenumber sampling will be described.

4.5.1 Fast Field Approximation

It has been shown that except for ranges shorter than a few wavelengths and very steep propagation angles, accurate evaluation of the inverse Hankel transform, Eq. (4.93), can be obtained by the so-called FFP (Fast Field Program) integration technique intro-

duced by DiNapoli and Deavenport [1].

First the Bessel function is expressed in terms of Hankel functions,

$$J_m(k_r r) = \frac{1}{2}\left[H_m^{(1)}(k_r r) + H_m^{(2)}(k_r r) \right] , \tag{4.94}$$

where $H_m^{(1)}$ with the present choice of the time–frequency transform corresponds to outgoing waves and $H_m^{(2)}$ to incoming waves. This latter term is important only for representing the standing wavefield at very short ranges and is therefore neglected. Next we replace $H_m^{(1)}(k_r r)$ by its asymptotic form [30],

$$\lim_{Kr \to \infty} H_m^{(1)}(k_r r) = \sqrt{\frac{2}{\pi k_r r}}\, e^{i\left[k_r r - (m + \frac{1}{2})\frac{\pi}{2} \right]} , \tag{4.95}$$

to arrive at the following expression for the inverse Hankel transform,

$$g(r, z) \simeq \sqrt{\frac{1}{2\pi r}}\, e^{-i\left(m + \frac{1}{2}\right)\frac{\pi}{2}} \int_0^\infty g(k_r, z)\, \sqrt{k_r}\, e^{ik_r r} dk_r . \tag{4.96}$$

The approximation of Eq. (4.93) by Eq. (4.96) has not removed any of the complications concerning the integration interval or the oscillatory nature of the integrand. However, the exponential function is more suitable for numerical integration than the Bessel function, particularly in terms of computation time. Since the numerical implementations used in underwater acoustics are almost without exception based on the fast-field approximation, we will focus on the evaluation of this integral in the following. It should be pointed out, however, that the truncation and sampling considerations discussed here apply as well to any direct numerical evaluation of Eq. (4.93).

4.5.2   Truncation of Integration Interval

To numerically evaluate the FFP integral, Eq. (4.96), we must either use a quadrature scheme for semi-infinite integration intervals or truncate the integration interval at a wavenumber beyond which the contribution to the integral is insignificant.

Although the first approach seems desirable in terms of accuracy, it is rarely used in the numerical implementations of the wavenumber integration approaches in underwater acoustics and seismology. The reason is in part that such a quadrature scheme would have to incorporate the oscillation of the exponential function in Eq. (4.96), which is different for the various ranges considered. It would therefore lead to different quadrature points for each range, with a significant additional computational effort as a result. Secondly, the variation of the kernel is strongly dependent on the environmental model and frequency, and moreover characterized by features such as poles and branch cuts not suited for quadrature schemes for infinite intervals.

Instead, the wavenumber axis is truncated, allowing for numerical quadrature without the complication of a semi-infinite integration interval. The reason for this approach being applicable is that the kernel in general decays very rapidly beyond a certain wavenumber $k_{\max}$. For example, consider the depth-dependent solution for the Pekeris waveguide, Eq. (2.159), consisting of a source contribution and two homogeneous solutions. For large values of the horizontal wavenumber, the exponential functions all have real arguments, corresponding to evanescent waves with an exponential decay in depth. It is easily verified that in the source layer, the source term will have the slowest decay rate for large wavenumbers. Thus, for large source–receiver separations in depth, the integration kernel will be rapidly decaying with increasing k_r. For small separations the decay is slower, and in the extreme situation of source and receiver at the same depth, the kernel only decays as k_r^{-1} for $k_r \to \infty$. Based on this information, it is usually straightforward to truncate the integration interval to obtain any degree of accuracy, except for the extreme case mentioned above where additional measures must be taken. Of course, it is desirable also for computational reasons to limit the integration interval as much as possible.

In order to appropriately truncate the integration interval, we can take advantage of the oscillatory nature of the exponential function in Eq. (4.96). Thus, for $r \neq 0$ it will ensure the convergence of the integral for $k_r \to \infty$, even for source and receiver at the same depth where the kernel alone is non-integrable. Therefore, the contribution to the integral beyond a certain wavenumber $k_{\max}$ will be negligible. However, $k_{\max}$ will depend on range, and for multiple ranges it is not desirable to truncate at different wavenumbers, instead it is desirable to have a wavenumber interval which is independent of range. An easy solution is to taper the kernel close to the maximum wavenumber selected such that the kernel is forced to gradually vanish over a wavenumber interval where the exponential function oscillates over several periods [13].

It should be stressed, that although the tapering of the kernel can be used to eliminate truncation errors, the actual choice of $k_{\max}$ is not easily automated. On the contrary, a proper choice usually requires a fundamental understanding of waveguide acoustics, in particular for elastic bottoms and ice covers, where significant components of the field have propagation wavenumbers far out in the evanescent regime.

4.5.3 Wavenumber Discretization - Aliasing

To numerically evalute the wavenumber integral in Eq. (4.96) the integration kernel must be evaluated at a discrete number of wavenumbers. Even though dedicated quadrature schemes may be devised for certain canonical problems, the truncated wavenumber space in general is discretized equidistantly,

$$k_\ell = k_{\min} + \ell \, \Delta k_r \,, \qquad \ell = 0, 1 \ldots (M-1) \,, \tag{4.97}$$

where M is the total number of sample points, and $\Delta k_r = (k_{\max} - k_{\min})/(M-1)$. Inserting Eq. (4.97) in Eq. (4.96) then yields the discrete wavenumber representation of the field integral

$$g^*(r, z) = \frac{\Delta k_r}{\sqrt{2\pi r}} \, e^{i\left[k_{\min}r - (m+\frac{1}{2})\frac{\pi}{2}\right]} \sum_{\ell=0}^{M-1} \left[g(k_\ell, z)\sqrt{k_\ell}\right] e^{i\ell\Delta k_r r} , \qquad (4.98)$$

It is well known from the discretization of time–frequency transforms that under-sampling in one domain causes aliasing (wrap-around) in the other domain (see e.g., Ref. [31], Sec. 3.2), and being a Fourier transform, the wavenumber integral is exposed to the same problem.

However, as will be discussed in the following, this aliasing problem is directly related to the periodicity of the exponential functions, and its effect can in fact be quantified, and remedies be designed to reduce its effect to insignificance. The Fast Field approximation to the wavenumber integral, Eq. (4.96) can be written in the form

$$g(r, z) \simeq h(r)f(r, z), \qquad (4.99)$$

with $h(r)$ representing the range-dependent amplitude and phase factor

$$h(r) = \sqrt{\frac{1}{2\pi r}} \, e^{-i\left(m+\frac{1}{2}\right)\frac{\pi}{2}} \qquad (4.100)$$

and $f(r, z)$ representing the wavenumber integral

$$f(r, z) = \int_0^\infty g(k_r, z) \sqrt{k_r} \, e^{ik_r r} dk_r . \qquad (4.101)$$

In this form, $f(r, z)$ represents the entire field variability except for the geometric spreading. Therefore, although the present analysis concerns a cylindrical geometry, the results apply directly to the plane problem, with the only change being elimination of the cylindrical spreading factor $r^{-1/2}$.

In analogy, the discrete form in Eq. (4.98) is written as

$$g^*(r, z) = e^{ik_{\min}r} h(r)f^*(r, z), \qquad (4.102)$$

with $f^*(r, z)$ representing the discrete summation evaluation of the wavenumber integral

$$f^*(r, z) = \Delta k_r \sum_{\ell=0}^{M-1} g(k_\ell, z) \sqrt{k_\ell} \, e^{ir\ell\Delta k_r} . \qquad (4.103)$$

In this form it is clear that adding $R = 2\pi/\Delta k_r$ to the range r simply adds an integer multiple of 2π to the argument of the exponential function. Equation (4.103) therefore yields a periodic solution,

$$f^*(r + nR, z) \equiv f^*(r, z), \ n = -\infty, \ldots, 0, \ldots \infty. \tag{4.104}$$

Therefore, whereas the continuous integral represents a solution over an infinite range interval, the discrete summation in Eq. (4.103 represents a solution over a limited range window $r = [r_{\min}, r_{\min} + R]$, with the solution at all other ranges being determined through the periodicity condition in Eq. (4.104).

In addition, since adding $R = 2\pi/\Delta k_r$ to the range simply adds an integer multiple of 2π to the argument of the exponential function, Eq. (4.103) also constrains the field and all its derivatives to be continuous at all the window boundaries, $r = r_{\min} + nR, n = -\infty \ldots \infty$. This property is the true culprit of the aliasing problem.

Thus, consider the problem of computing the field produced by a physical source at the origin $r = 0$ iun a Pekeris waveguide. The integration kernel $g(k_r, z)$ is shown schematically in the upper frame in Fig. 4.5, with the dashed portion near the origin indicating the squareroot singularity introduced by the geometric $\sqrt{k_r}$ factor. Because of the continuity condition at range window boundaries $r = nR$, all wave components produced by the physical source in the range window $n = 0 : [0, R]$, propagating in the positive direction at $r = R$, must be matched by identical wave components propagating in the positive direction in the neighboring window $n = 1 : [R, 2R]$. Because of the periodicity these wave components will therefore also exist in in the current window $n = 0$, where they will appear to be originating from sources in the previous range window $n = -1$. Similarly, if the Hankel function in Eq. (4.94) representing the incoming components were retained as will be the case in the *Fast Hankel Transform* described later in Sec. 4.5.6, all wave components propagating in the negative direction at $r = 0^+$ also will have to appear as negatively propagating waves at $r = R^-$, appearing to originate at the periodic source at $r = R^+$ in the neighbor window $n = 1$. Even though these components are ignored here, the positive wavenumbers will contribute at small negative ranges, as indicated in the figure, yielding a non-vanishing field which will also wrap into the current window at $r = R$.

Similarly, if the true field extends beyond the neighbor windows, the field from the virtual sources in these windows will be wrapped into the current window as well. As a consequence the field represented by the Fourier summation in Eq. (4.103) will be the *superposition* of the field produced by an infinity of *periodic sources*, with the resulting field being

$$g^*(r, z) = e^{ik_{\min}r} h(r) f^*(r, z) = h(r) \sum_{n=-\infty}^{\infty} f(r + nR, z), \tag{4.105}$$
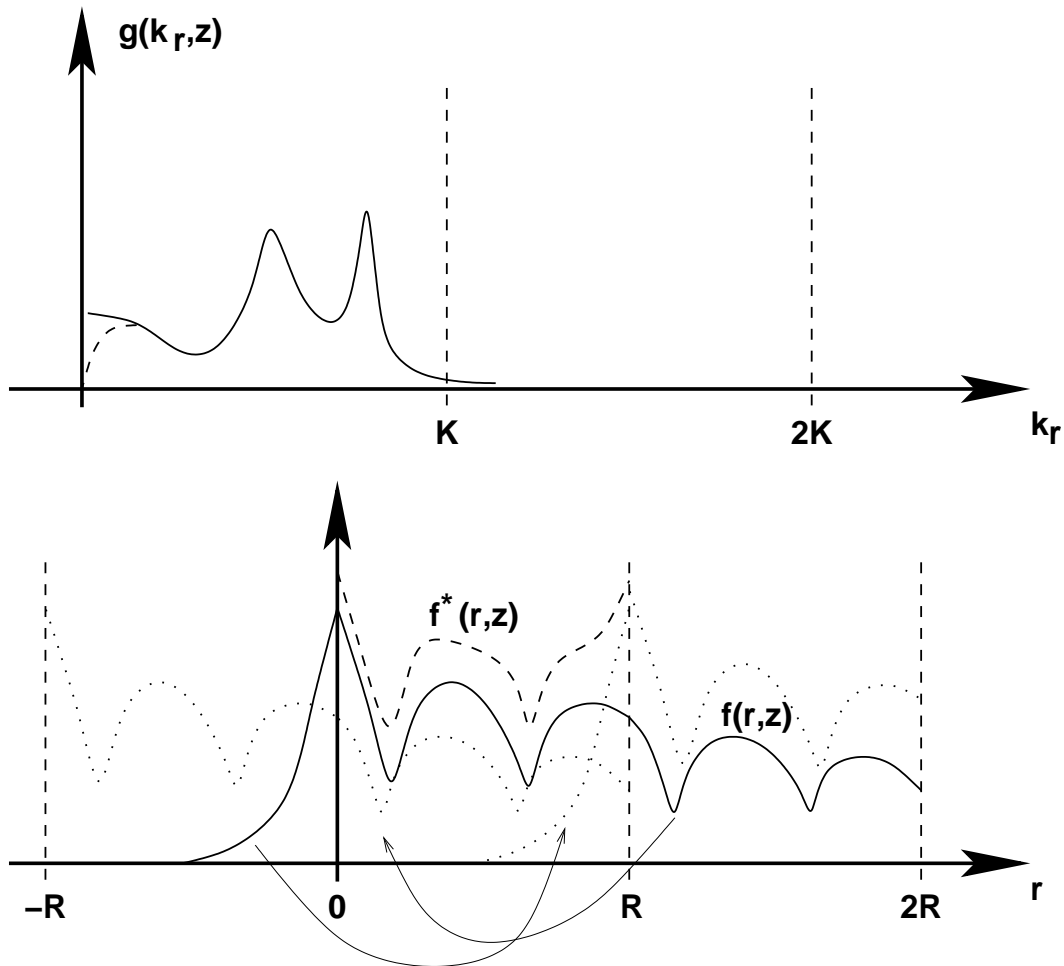
Fig. 4.5. Aliasing associated with discrete wavenumber integration for typical Pekeris wave-guide problem. The wavenumber kernel showing the presence of a two attenuated modes is sketched in the upper plot, with the squareroot singularity introduced by the geometric $\sqrt{k_r}$ indicated by the dasjhed curve near the origin. The discrete wavenumber integration yields the periodic result shown in the lower frame by a dashed curve, approximating the correct continuous result shown as a solid curve. The discrete result is a superposition of the 'true' field produced by the mirror sources in all the range windows.

where $f(r, z)$ represents the true field as represented by the continuous integral, Eq. (4.96).

Thus, in summary the discretization of the wavenumber integral forces a periodic solution, with the inherent property that the discrete fourier transform $f^*(r, z)$ in each range window of width R is a superposition of the 'true' field $f(r, z)$ produced by an infinite number of periodic source 'images', as illustrated in Fig. 4.5.

As a consequence, for the discrete wavenumber integral to be correct, the field produced by each source must vanish outside the range interval considered, otherwise it will be wrapped into the neighboring windows, and vice versa for the sources in the neighbor windows. This is the fundamental aliasing or wrap-around problem associated with discrete Fourier Transforms, requiring the range window to be large enough for the periodic components to be insignificant, in turn requiring the wavenumber sampling, to be small. On the other hand, if the signal dies out before reaching the neighboring window, the discrete form will be approaching the exact solution. In the cylinder analogy this corresponds to a wave field which is attenuated enough to reduce the periodic multiples to insignificance.

Because of the two-sided nature of the discrete Fourier transform, aliasing occurs from both sides of the actual interval and therefore also from ranges smaller than $r_{\min}$. If $r_{\min} > 0$ the strong signals in the interval $[0, r_{\min}]$ are wrapped into the interval $[R, r_{\min} + R]$. Therefore *the maximum range is always $R = 2\pi/\Delta k_r$, independent of the choice of $r_{\min}$.*

4.5.4 FFP: Fast Field Program

The field solution is often required at a large number of ranges r_j, in particular in connection with the common underwater acoustics problem of determining transmission loss as function of range. In these cases the Fourier series summation in Eq. (4.103) is very efficiently evaluated by means of an FFT (Fast Fourier Transform). In this Fast-Field-Program (FFP) approach introduced by DiNapoli and Deavenport [1] the range axis r is discretized as

$$r_j = r_{\min} + j\,\Delta r\,, \qquad j = 0, 1 \ldots (M-1)\,, \tag{4.106}$$

where the range step Δr is constrained by the wavenumber discretization through the relation

$$\Delta r\,\Delta k_r = \frac{2\pi}{M}\,, \tag{4.107}$$

and M is an integral power of 2. The following discrete approximation of Eq. (4.96) is then obtained,

$$g^*(r_j, z) = \frac{\Delta k_r}{\sqrt{2\pi r_j}}\, e^{i\left[k_{\min}r_j - \left(m+\frac{1}{2}\right)\frac{\pi}{2}\right]} \sum_{\ell=0}^{M-1} \left[g(k_\ell, z)\, e^{ir_{\min}\ell\,\Delta k_r}\sqrt{k_\ell}\right] e^{i\frac{2\pi\ell j}{M}}\,, \tag{4.108}$$
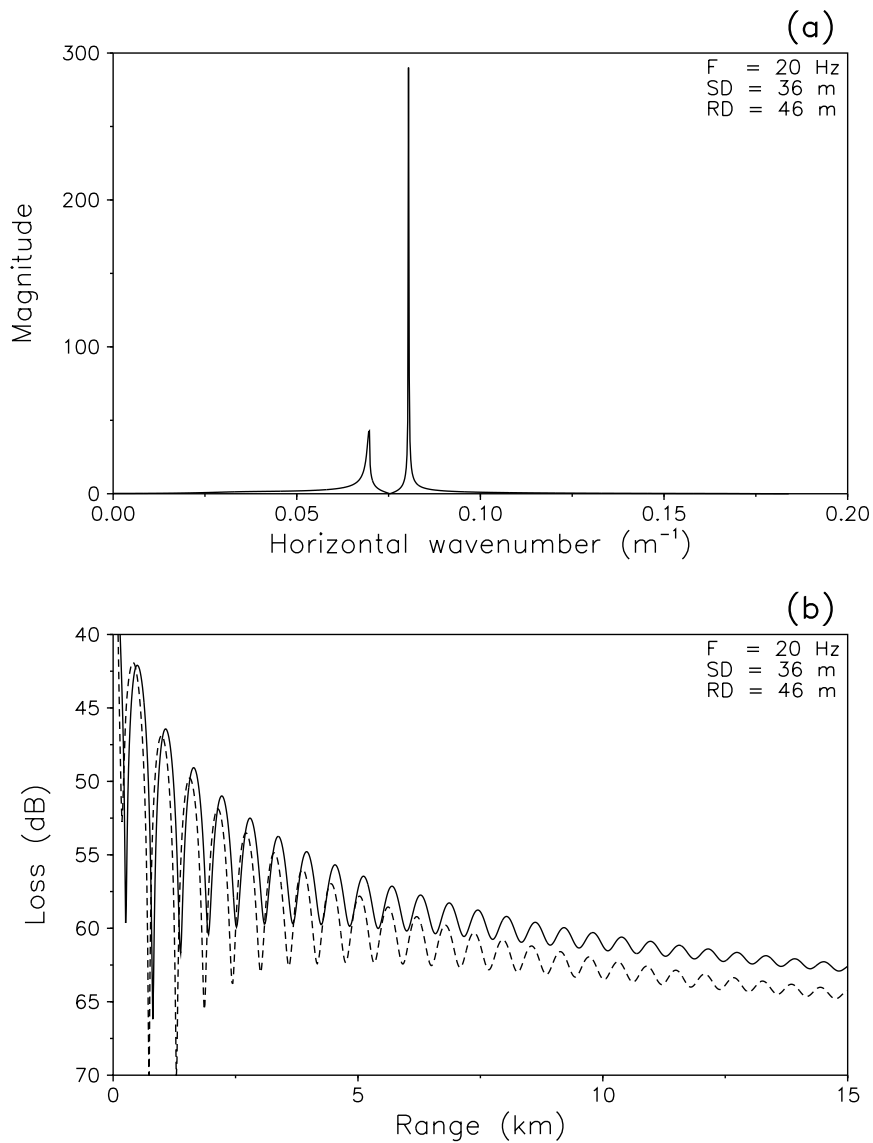
Fig. 4.6. Acoustic field at 46-m depth in a Pekeris waveguide with a water speed of 1500 m/s and a bottom speed of 1800 m/s. **(a)** Magnitude of integration kernel along real wavenumber axis. **(b)** Transmission loss. Solid curve: Exact solution. Dashed curve: Real-axis FFP integration with $k_{max} = 0.2\,\mathrm{m}^{-1}$ and 1024 sample points.

where the summation can be performed by means of an FFT, yielding the field at all M ranges simultaneously.

Note here that

$$e^{i(-\ell\Delta k_r)(j\Delta r)} = e^{i(2\pi j - \ell\Delta k_r(j\Delta r))} = e^{i(M-\ell)\Delta k_r(j\Delta r)}. \tag{4.109}$$

Therefore, for $k_{\min} = 0$ the upper half of the wavenumber components in Eq. 4.103 is indistinguishable from the negative wavenumbers in regard to the value of the exponential, such that, even though the original integral in Eq. 4.98 was one-sided, the summation is equivalent to a two-way propagation problem. With $r_{\min} = 0$ this makes the discrete approximation of the wavenumber integral valid only up to a range $r = R/2$, consistent with the *Nyquist* sampling criterion [31]. Here, however, the one-sided nature of the original integral in Eq. (4.96) may yield a solution which is valid at ranges longer than the Nyquist range. Thus, with only positive wavenumbers considered, the wrap-around of the negative spectrum will correspond to the wavenumbers $k_r > M\Delta k_r/2$. Therefore, as illustrated in Fig. 4.5, one can choose a wavenumber interval $[0, 2K]$ such that the upper half is all beyond the significant evanescent components, reducing the negative spectrum wrap-around to insignificance, and the range of validity extended beyond $R/2$. However, as also illustrated in Fig. 4.5, the field will never vanish entirely at negative ranges, because of the finite contribution from the small wavenumber components, and more inportantly the numerical artifact of the discontinuity of the kernel at $k_r = [0, 2K]$. Even though the $\sqrt{k_r}$ factor introduced by the FFP approximation forces the kernel to vanish, the derivatives remain discontinuous, and an artificial backward propagating field will result, which will be wrapped into the current range window near $r = R$ as illustrated in the figure. Therefore, even though a simple zero-padding at large wavenumbers is a computationally efficient method for extending the range beyond the Nyquist limit $R/2$ it is not in general recommendable. Instead, the range should be extended by simply reducing the wavenumber sampling Δk_r.

We will illustrate the effect of aliasing by using the FFP integration scheme, Eq. (4.108), to evaluate the transmission loss versus range at 46-m depth in the Pekeris waveguide shown in Fig. 2.25. The source depth is 36 m and the frequency 20 Hz. The magnitude of the integration kernel along the real wavenumber axis is shown in Fig. 4.6(a). Since an attenuation of $0.5\,\text{dB}/\lambda$ is assumed in the bottom, no poles exist on the real axis, but the pole corresponding to the first propagating mode is evident as an extremely sharp peak. Figure 4.6(b) shows the exact transmission loss out to a range of 15 km as the solid curve. The dashed curve is the FFP result obtained by integrating the kernel in Fig. 4.6(a) using 1024 sample points equidistantly spaced between $k_{\min} = 10^{-9}\,\text{m}^{-1}$ and $k_{\max} = 0.2\,\text{m}^{-1}$, i.e., $\Delta k_r = 2 \times 10^{-4}\,\text{m}^{-1}$, corresponding to a range window $R = 2\pi/\Delta k_r \simeq 30\,\text{km}$. The aliasing due to undersampling of the sharp

peak in Fig. 4.6(a) clearly introduces errors of up to 2 dB in the predicted transmission loss, with the largest errors at longer ranges. However, even at short ranges the aliasing introduces errors in the modal interference pattern.

4.5.5   Complex Contour Integration

The aliasing from ranges larger than $r_{\min} + R$ can be reduced by choosing R so large that the signal is known to die out within the range window. Here it is important to note that the cylindrical spreading of the point-source waveguide field is accounted for by the $r^{-1/2}$ factor in Eq. (4.100). As described above, the wrap-around is purely an effect of the replacement of the integral by the summation in Eq. (4.103), and to avoid the wrap-around it is necessary that the field decays more rapidly with range than the geometrical spreading decay $r^{-1/2}$. For a perfectly lossless waveguide, the modal field decays only due to geometrical spreading. Consequently, the range window cannot in this case be made large enough to eliminate the wrap-around, which is consistent with the fact that the normal modes appear as singularities on the real wavenumber axis, and these poles can never be properly sampled.

Therefore, direct numerical evaluation of the wavenumber integral in Eq. (4.96) is possible only for waveguides with some form of attenuation. In the real ocean, both the water and the bottom have a finite volume attenuation, but in particular for environments with little bottom interaction, the attenuation loss is very small. In these cases a large range window, and therefore very fine wavenumber sampling, must be chosen to avoid wrap-around. This is clearly undesirable for computational reasons, particularly in cases where the field is needed only at relatively short ranges.

The aliasing problem can, however, be eliminated by moving the integration contour out into the complex plane. According to *Cauchy's theorem* the integral in the complex plane between two points is invariant to a change in the integration contour. Therefore Eq. (4.96) can be replaced by

$$g(r, z) \simeq h(r)f(r, z) = h(r) \int_C g(k_r, z) \sqrt{k_r} \, e^{ik_r r} \, dk_r \,, \qquad (4.110)$$

where C is the contour shown in Fig. 4.7. The contour consists of three linear sections C_1, C_2, and C_3, where the vertical sections of length ϵ are chosen at the points where the wavenumber axis would in any case be truncated. If these points are chosen where the kernels are small, i.e., where $g(k_{\min}, z) \sqrt{k_{\min}} \simeq 0$, $g(k_{\max}, z) \sqrt{k_{\max}} \simeq 0$, and $\epsilon \ll k_{\max} - k_{\min}$, then the contributions from the vertical sections become insignificant compared to the integral along the horizontal section defined by $\widetilde{k} = k - i\epsilon$. By inserting $\widetilde{k}$ in Eq. (4.110), we obtain

$$g(r, z) \simeq h(r)f(r, z)$$
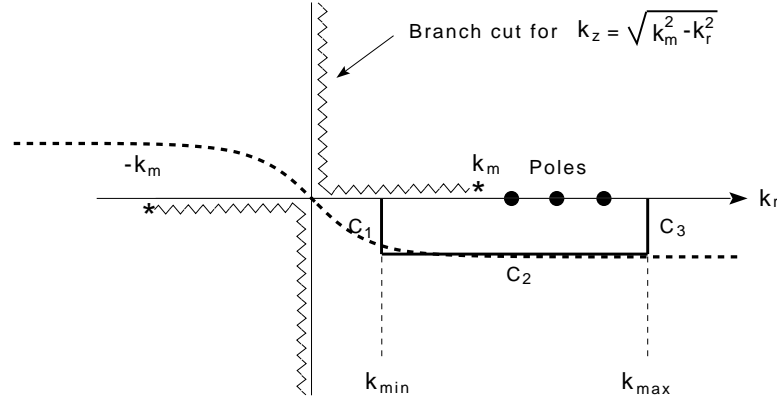
Fig. 4.7. Complex integration contours for evaluation of wavenumber integral. The contour C2 is used for FFP integration, while the 'exact' hyperbolic tangent contour indicated by the dashed line is used for trapezoidal rule integration

$$= h(r) \int_{k_{\min}}^{k_{\max}} g(k_r - i\epsilon, z) \sqrt{k_r - i\epsilon} \; e^{i(k_r - i\epsilon)r} \, dk_r \, . \qquad (4.111)$$

which after multiplication by $e^{-\epsilon r}$ takes the form

$$g(r, z) \, e^{-\epsilon r} \; \simeq \; h(r) f(r, z) \, e^{-\epsilon r}$$

$$= \; h(r) \int_{k_{\min}}^{k_{\max}} g(k_r - i\epsilon, z) \sqrt{k_r - i\epsilon} \; e^{ik_r r} \, dk_r \, . \qquad (4.112)$$

As described above a periodic approximation to the integral in Eq. (4.112) can be determined by means of an FFT, with the result

$$g(r_j) f(r_j, z) e^{-\epsilon r_j} = e^{ik_{\min}r_j - \epsilon r_j}$$

$$= h(r_j) \sum_{n=-\infty}^{\infty} f(r_j + nR, z) e^{-\epsilon(r_j + nR)}$$

$$\simeq \Delta k_r e^{ik_{\min}r} h(r_j) \sum_{\ell=0}^{M-1} \left[g(k_\ell - i\epsilon, z) \, e^{ir_{\min}\ell \Delta k_r} \sqrt{k_\ell - i\epsilon} \right] e^{i\frac{2\pi \ell j}{M}} \quad (4.113)$$

or, after multiplication with $e^{\epsilon r_j}$, rearrangement of terms, and use of the Eq. (4.99),

$$g(r_j, z) \; \simeq \; h(r_j) f(r_j, z)$$

$$= \; \Delta k_r e^{(\epsilon + ik_{\min})r_j} h(r_j) \sum_{\ell=0}^{M-1} \left[g(k_\ell - i\epsilon, z) \, e^{ir_{\min}\ell \Delta k_r} \sqrt{k_\ell - i\epsilon} \right] e^{i\frac{2\pi \ell j}{M}}$$

$$- h(r_j) \sum_{n \neq 0} f(r_j + nR, z) \, e^{-\epsilon n R} \, . \tag{4.114}$$

In this form it is clear that all signals wrapped around from ranges larger than $r_{\min} + R$ will be attenuated by at least $\exp(-\epsilon R)$. On the other hand, signals wrapped around from ranges smaller than $r_{\min}$ will be amplified by at least $\exp(\epsilon R)$. As was the case for the real-axis integration, the maximum range is therefore $r_{\max} = R$ also for the offset contour integration.

The explanation for this is as follows. The contour offset moves the integration path away from singularities such as branch points and modes resulting in a similar but smoother integration kernel. It is well known that a smoother kernel yields a more rapidly decaying Fourier transform, corresponding to adding an artificial attenuation in range, and the corresponding field is therefore less likely to wrap into the neighboring range window. The multiplication of the transform result by the spatial exponential $e^{\epsilon r}$ compensates for this artificial attenuation and restores the correct field decay with range.

The actual value of ϵ is not extremely critical. However, if it is chosen too large the contributions from the two vertical parts of the contour may become significant. On the other hand, a too small value will require a very large number of sampling points. For most practical purposes an attenuation of the wrap-around by 60 dB is more than sufficient [13]. The corresponding value of the *contour offset* is

$$\epsilon = \frac{3}{R \log e} = \frac{3}{2\pi \, (M - 1) \log e} \, (k_{\max} - k_{\min}) \, , \tag{4.115}$$

which even for a relatively small number of sample points M will ensure that $\epsilon \ll k_{\max} - k_{\min}$, and thus yield insignificant contributions from the vertical contours.

Figure 4.8 illustrates the effects of using the complex integration contour for evaluation of the field in the Pekeris waveguide treated above. Figure 4.8(a) shows the magnitude of the kernel of the summation in Eq. (4.114) for two contour offsets defined by Eq. (4.115). The solid curve is the kernel along a contour with an offset corresponding to $M = 1024$ sampling points in the wavenumber interval shown, whereas the dashed curve is the kernel for $M = 512$ sampling points over the same interval. When compared to Fig. 4.6(a), it is clear that the contour offset has a smoothing effect on the integration kernel, and also results in lower amplitudes as is evident at the poles in particular. The effect of the lower amplitudes is compensated by the exponential outside the summation in Eq. (4.114).

Figure 4.8(b) shows the transmission loss computed from Eq. (4.114) for the two contours. On the dB-scale used here, the loss computed with $M = 1024$ (solid curve) is identical in the whole range window to the exact loss shown as the solid curve in Fig. 4.4(b). However, the loss computed with $M = 512$ (dashed curve) is correct only
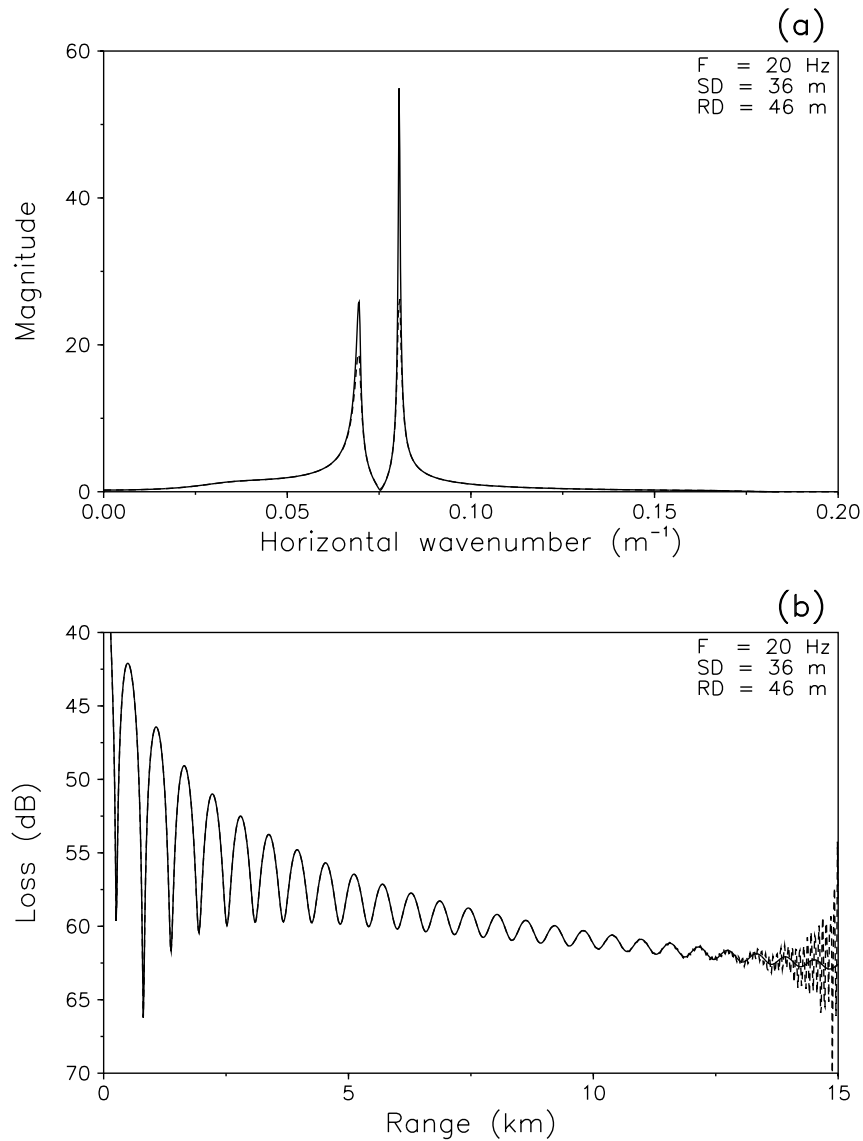
Fig. 4.8. Acoustic fi eld in a Pekeris waveguide computed with complex integration contours. **(a)** Magnitude of integration kernel along contours offset ϵ given by Eq. (4.115) with $k_{\max} = 0.2\,\text{m}^{-1}$, and $M = 1024$ (solid curve) and $M = 512$ (dashed curve). **(b)** Transmission loss computed with $M = 1024$ (solid curve) and $M = 512$ (dashed curve).

out to a range of approximately $10\,\text{km}$, after which the result shows increasing errors. These errors appear in spite of the fact that the maximum range for this sampling is $R = 2\pi/\Delta k_r \simeq 15\,\text{km}$. This is due to the fact that even though we have removed the negative wavenumber spectrum represented by the Hankel function $H_m^{(2)}(k_r r)$, the value of the integral in Eq. (4.110) does not vanish for negative ranges r. According to the arguments above, the field for negative r will therefore wrap into the actual window, magnified by at least $\exp(\epsilon R)$. However, these components decay rapidly with negative range, and the wrap-around will therefore be confined to ranges close to the maximum range R. In general, experience shows that the solution obtained from Eq. (4.114) is correct to within a fraction of a decibel at least out to the Nyquist range $r = R/2 = \pi/\Delta k_r$.

Whereas the fast-field integration is very efficient for single-frequency transmission loss calculations, its use is inconvenient in the case of wideband pulse calculations. If the pulse response is required at more than a single range, the wavenumber sampling distance Δk_r would have to be frequency independent in order to satisfy Eq. (4.107). Furthermore, since the pulse response is usually required only for a relatively small number of ranges, one of the direct numerical quadrature schemes described in the following is generally more efficient.

4.5.6   Fast Hankel Transforms

The Fast Field Program (FFP) approach described above has gained popularity because of its efficiency in producing field estimates at a large number of ranges. However, being based on the large argument asymptotic of the Hankel functions it is associated with errors for small arguments $k_r r$ of the Bessel function, i.e. for short ranges or small wavenumbers. Since the steep angles associated with small horizontal wavenumbers in general attenuates rapidly with range for typical ocean waveguides due to bottom interaction, and the FFP approach for practical purposes has therefore only been limited by range. On the other hand, the minimum range for which the error is acceptable is a complicated function of frequency and environment. Without full Hankel transform reference solutions there is no way of defining this limit of validity, and the use of the FFP has therefore been associated with a significant degree of uncertainty at short ranges, at low frequencies in particular. The same is of course the case for cases where the short range field is important, such as for seabed reverberation synthesis [26].

Even on todays computers the generation of Bessel functions is time consuming, and in general a direct, brute-force numerical integration technique for evaluating the Hankel transforms in Eq. (4.93) is not feasible. On the other hand algorithms are available for directly evaluating the Hankel transform, Eq. (4.93) using dedicated quadrature schemes. The one developed by Tsang *et al.* [24], however, requires the evaluation of

an FFT for every receiver range, but, more importantly, it requires a numerical separa-
tion parameter which is not easily selected. The so-called Fast Hankel Transform [25]
is very efficient for relatively smooth kernels, but not well-suited for the rapidly vary-
ing kernels of waveguide problems. More efficient *Fast Hankel Transforms* have been
developed recently [27, 28, 29], but they are in general restrictive in terms sampling
requirements and therefore not easily adapted to the ocean acoustics problem where
the sampling is controlled by the waveguide physics, and where the field is desired at
a predetermined grid of horizontal ranges. Being based on the FFT, the advantage of
the FFP technique described above is that it efficiently approximates the Hankel trans-
form on a regular grid of wavenumbers and ranges. However, it is possible to design
a numerically efficient correction to the FFP which allows for accurate accounting for
the small argument contributions.

The Hankel transform integrals are of the form

$$
\begin{aligned}
g(r) &= \int_0^\infty g(k_r) k_r J_m(k_r r) dk_r \\
&= \frac{1}{2} \int_0^\infty g(k_r) k_r \left[H_m^{(1)}(k_r r) + H_m^{(2)}(k_r r) \right] dk_r
\end{aligned}
\tag{4.116}
$$

where $H_m^{(1)}$ for $\exp -i\omega t$ time-dependence corresponds to outgoing waves and $H_m^{(2)}$ to
incoming waves, both of azimuthal fourier order m dependence. For classical acoustic
forward propagation modeling the incoming waves are ignored, eliminating the second
term. However, for short range, and for backscattering problems, for example, it must
be retained. Next the Hankel functions $H_m^{(1,2)}(k_r r)$ by their asymptotic form [30],

$$
\lim_{kr \to \infty} H_m^{(1,2)}(k_r r) = \sqrt{\frac{2}{\pi k_r r}} \, e^{\pm i[k_r r - (m + \frac{1}{2})\frac{\pi}{2}]} ,
\tag{4.117}
$$

to arrive at the following approximation to the Hankel transform,

$$
g(r) \simeq g^*(r) = \sqrt{\frac{1}{2\pi r}} \int_0^\infty g(k_r) \sqrt{k_r} \left[e^{i[k_r r - (m + \frac{1}{2})\frac{\pi}{2}]} + e^{-i[k_r r - (m + \frac{1}{2})\frac{\pi}{2}]} \right] dk_r
\tag{4.118}
$$

This integral can be rewritten as a two-sided Fourier transform,

$$
g^*(r) = \int_{-\infty}^\infty f(k_r) e^{ik_r r} dk_r ,
\tag{4.119}
$$

with the kernel

$$
f(k_r) = \begin{cases} g(-k_r)\sqrt{\frac{-k_r}{2\pi r}} e^{i(m + \frac{1}{2})\frac{\pi}{2}} & k_r < 0 \\ g(k_r)\sqrt{\frac{k_r}{2\pi r}} e^{-i(m + \frac{1}{2})\frac{\pi}{2}} & k_r \geq 0 \end{cases}
\tag{4.120}
$$
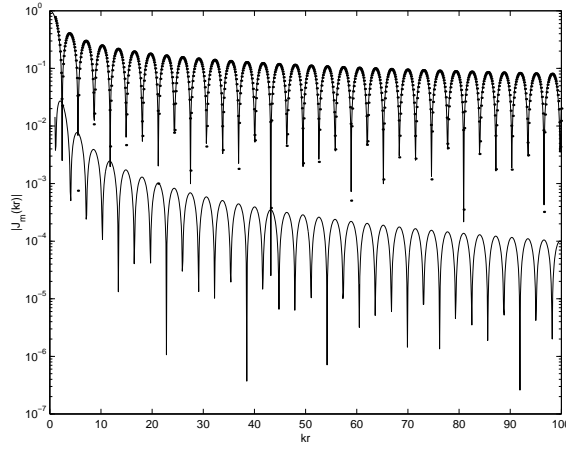
Fig. 4.9. Error of far-field approximation of $J_0(kr)$. Solid: Exact. Dots: Large-argument approximation, Dashed: Error.

Similarly to the FFP discussed above, Eq. (4.119) is efficiently evaluated using a standard Fast Fourier Transform if the range r and wavenumber k are discretized equidistantly, with the sampling intervals being constrained by Eq. 4.107.

The error associated with using Eq. (4.119) is clearly associated with the approximation of the Bessel function in terms of the asymptotic expressions of the Hankel functions. Figure 4.9 shows the exact absolute value of the Bessel function $J_0(k_r r)$ for $k_r r \leq 100$ as a solid curve and the asymptotic values indicated by the dots. The absolute error is indicated by the dashed curve, and it is clear that the error of the approximation is less than 10^{-4} for $k_r r \geq 20\pi$. Consequently, to achieve a more accurate evaluation of the Hankel Transforms of order 0 in Eq. (4.93) it is only necessary to correct the contributions corresponding to values of $k_r r \leq KR = 20\pi$. This is performed in a numerically stable manner by a Hanning weighted average of the contributions of the exact Bessel function and the approximate FFP kernel,

$$g(r) = g^*(r) + \int_0^{KR} g(k_r) w(k_r r) [k_r J_0(k_r r)$$

$$- \sqrt{\frac{k_r}{2\pi r}} \left(e^{i(k_r r - (m+\frac{1}{2})\frac{\pi}{2})} + e^{-i(k_r r - (m+\frac{1}{2})\frac{\pi}{2})} \right)] dk_r \qquad (4.121)$$

where the tapered weight function $w(kr)$ is

$$w(k_r r) = \begin{cases} 1 & k_r r \leq KR/2 \\ [1 + \cos(\pi(kr - KR/2)/(KR/2))]/2 & KR/2 < k_r r < KR \end{cases} \qquad (4.122)$$

Equation (4.121) can be evaluated very efficiently. First of all, with the wavenumber and range sampling constrained by Eq. (4.107), all values of the exponentials are computed as part of the FFT evaluation of Eq. (4.118). Secondly, the Bessel functions will only be needed for a limited number of discrete values of the argument,

$$kr = n\Delta k_r \Delta r, \quad n = 0, \ldots \mathrm{KR}/(\Delta k_r \Delta r) , \tag{4.123}$$

which can be pre-computed into a look-up table.

As all other discrete wavenumber integration approaches, the present Fast Hankel Transform is susceptible to aliasing and wrap-around as described earlier in Sec. 4.5.3. However, the fact that the negative wavenumber spectrum is included makes the aliasing issue slightly different, as illustrated in Fig. 4.10. The full Hankel transform inherently contains both forward (positive) and backward (negative) propagating wavenumber components, with the real argument Bessel function in Eq. (4.93) representing the superposition of the two. The FFP $\sqrt{k_r}$ effect is again shown near the origin as a dashed curve section, but this geometric artifact is obviously replaced by the true Bessel function by the algorithm. As illustrated in Fig. 4.10 the inherent symmetry (symmetric kernels for m even, antisymmetric for m odd) in the wavenumber integral yiels a symmetric (or antisymmetric) sulution in each range window. Therefore the forward and backward wrap-around will be of the same order of magnitude, and the field approximation will be symmetric within each range window. Consequently the maximum range of validity is always the Nyquist range $r_{\max} = R/2 = \pi/\Delta k_r$ for the full Hankel Transform methods, assuming of course that R is choosen large enough to make the wrap-around insignificant in this part of the range window.

The performance of this 'Fast Hankel Transform' is illustrated by Fig. 4.11, which shows the evaluation of the Hankel transform

$$p(r, z) = \int_0^\infty \frac{e^{ik_z |z|}}{ik_z} k_r J_0(k_r r) dk_r \tag{4.124}$$

representing the free-field point source field. $k_z = \sqrt{(\omega/c)^2 - k_r^2}$ is the vertical wavenumber at angular frequency ω. Figure 4.11(a) shows the FFP approximation which clearly breaks down at steep angles and short ranges, while Fig. 4.11(b) shows the correct spherical spreading behavior at all propagation angles produced using Eq. (4.121).

4.5.7   Trapezoidal Rule Integration

For propagation problems involving a rela6tively small number of receivers, such as a vertical line array for matched field processing (see Chap. 10), or broad-band time simulations, the FFT-based techniques are not computationally attractive. On the contrary, the sampling constraint in Eq. (4.107 has to be combined with the geometric of
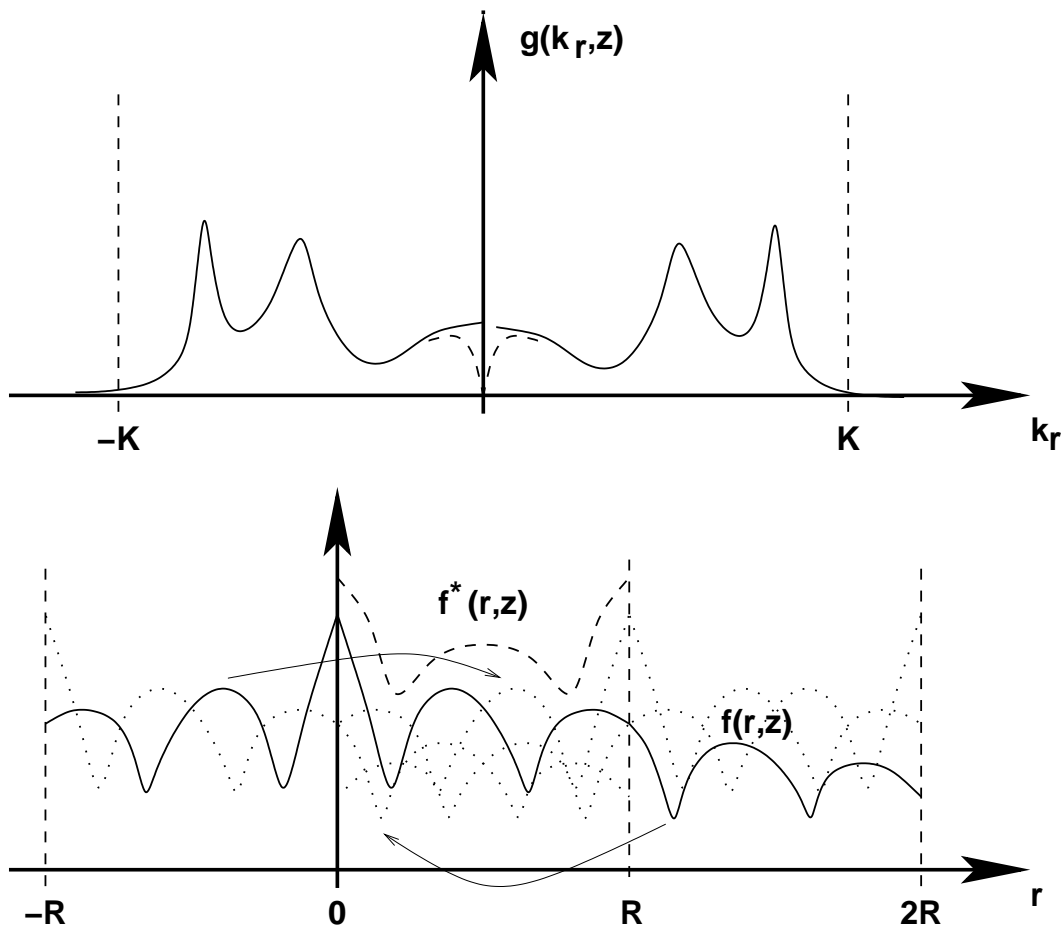
Fig. 4.10. Aliasing associated with Fast Hankel Transform integration for typical Pekeris wave-guide problem. The symmetric wavenumber kernel showing the presence of a two attenuated modes is sketched in the upper plot, with the $\sqrt{k_r}$ introduced by the FFP approximation indicated by the dashed curve near the origin. The discrete wavenumber integration yields the periodic result shown in the lower frame by a dashed curve, approximating the correct continuous result shown as a solid curve. The discrete result is a superposition of the 'true' field produced by the mirror sources in all the range windows.
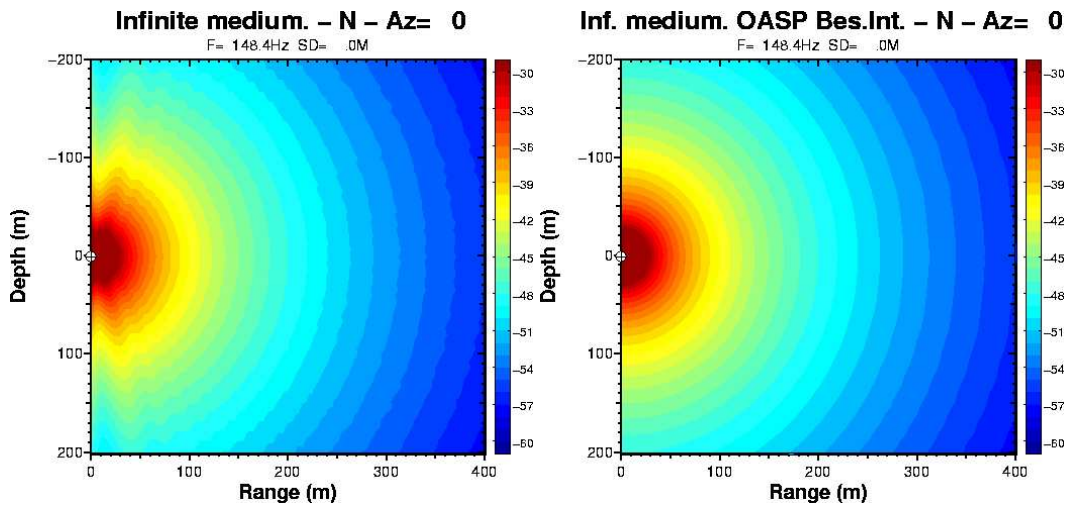
Fig. 4.11. Acoustic point source fi eld. (a) shows the FFP approximation which clearly breaks down at steep angles and short ranges, while (b) shows the correct spherical spreading behavior at all propagation angles, produced using Eq. (4.121)

the array, often requiring a wavenumber sampling which is fixed for all frequencies, which is not optimal.

As a consequence broad-band and discrete array computations are in general optimally being performed by direct numerical quadrature schemes such as the trapezoidal rule integration. This scheme approximates the integrand by a function varying linearly between the sampling points, and hence is applicable only out to ranges where the product of the kernel and the exponential function is well represented by a linear function. The kernel can be smoothed by moving the contour out into the complex plane as described above, but the exponential function varies rapidly for long ranges. To ensure that the exponential function alone is well represented by a linear function, the wavenumber sampling must satisfy the following inequality [32],

$$\Delta k_r \, R < \frac{\pi}{4} \, , \tag{4.125}$$

which by comparison with Eq. (4.107) translates into a maximum range which is much shorter than the one obtained by the fast-field technique. However, for equidistant sampling, the trapezoidal rule yields a result which is identical to Eq. (4.108), except for insignificant differences at the ends of the integration interval. It should be pointed out, however, that the FFP technique has a degraded accuracy at longer ranges, which is insignificant on the logarithmic scale used for displaying transmission loss, but it may become important in connection with wideband pulse calculations. For accurate pulse

calculations the maximum ranges for the two techniques are identical and determined by Eq. (4.125).

In addition to allowing frequency-dependence of the wavenumber sampling, another advantage of the direct numerical integration schemes is that they less restricted in terms of the wavenumber integration contour, even though they are obviously susceptible to the same aliasing problems. Thus, for example they do not have to use an integration contour parallel to the real axis such as the contour C_2 in Fig. 4.7, but can instead apply an 'exact' Cauchy contour such as the one shown by the dashed line in Fig. 4.7, totally eliminating the contributions from the two vertical contour sections. This is particularly important for short range problems where the contour C_1 becomes significant. Dawson and Fawcett [39] suggested the hyperbolic tangent contour for use with trapezoidal rule integration. The following contour is found to work well for most ocean acoustic and seismic problems,

$$\overline{k}_r = \begin{cases} k_r (1 - i\epsilon \tanh k_r/6\Delta k_r), & k_r/6\Delta k_r \leq 20 \\ k_r (1 - i\epsilon), & k_r/6\Delta k_r > 20, \end{cases} \quad (4.126)$$

where the asymptotic offset ϵ is given by Eq. (4.115).

Also, with its relatively small additional computational cost, it is strongly suggested to use the Fast Hankel Transform approach described in Section 4.5.6, but obviously implemented in a modified form, without using an FFT. Thus, Eq. (4.121) is easily re-arranged into a form directly suitable for trapezoidal rule integration, for the omni-directional field components, $m = 0$:

$$g(r) = \int_0^\infty g(k_r)[w(k_r r)k_r J_0(k_r r)$$

$$+ (1 - w(k_r r))\sqrt{\frac{k_r}{2\pi r}} \left(e^{i(k_r r - (m+\frac{1}{2})\frac{\pi}{2})} + e^{-i(k_r r - (m+\frac{1}{2})\frac{\pi}{2})}\right)]dk_r , \quad (4.127)$$

with the weight function

$$w(k_r r) = \begin{cases} 1 & k_r r \leq 10\pi \\ [1 + \cos(\pi(kr - 10\pi)/(10\pi))]/2 & 10\pi < k_r r < 20\pi \\ 0 & k_r r > 20\pi \end{cases} \quad (4.128)$$

As before, the Bessel functions can be pre-computed on a fixed grid up to the maximum argument $k_r r = 20\pi$, with the values at any intermediate argument being determined by interpolation. Here it has been found that for all practical applications a sampling of $\pi/20$ is more than adequate if combined with 4th order Lagrange interpolation.

4.5.8 Filon Integration

While the trapezoidal rule integration is accurate only for ranges which satisfy Eq. (4.125) for the product of the kernel and the exponential function in Eq. (4.110), it is possible to obtain accurate solutions at longer ranges by applying the generalized Filon integration scheme [33],

$$\int_a^b f(k_r)\, e^{Sg(k_r)}\, dk_r = \begin{cases} \frac{\Delta k_r}{S\,\Delta g}\left[\Delta\left\{f e^{Sg}\right\} - \frac{\Delta f\,\Delta\{e^{Sg}\}}{S\,\Delta g}\right], & \Delta g \neq 0 \\[2mm] \frac{\Delta k_r}{2}\left[f(a)\, e^{Sg(a)} + f(b)\, e^{Sg(b)}\right], & \Delta g = 0\ , \end{cases} \tag{4.129}$$

where $\Delta f = f(b) - f(a)$, and similarly for the other functions. This quadrature scheme is exact for linear variations of the kernel $f(k_r)$ and of the exponent $g(k_r)$. In the present case $S = ir$ and $g(k_r) = k_r$, i.e., the exponent is inherently a linear function of k_r. For the equidistant sampling given in Eq. (4.97), it is easily shown that the Filon integration scheme leads to the following quadrature scheme for evaluation of the wavenumber integral in Eq. (4.110),

$$g(r_j, z) \simeq \frac{w_j}{\sqrt{2\pi r_j}}\, e^{i\left[k_{\min}r_j - (m+\frac{1}{2})\frac{\pi}{2}\right]} \sum_{\ell=0}^{M-1} \left[g(k_\ell, z)\, e^{ir_{\min}\ell\Delta k_r}\sqrt{k_\ell}\right] e^{i\frac{2\pi\ell j}{M}}. \tag{4.130}$$

Here w_j are the range-dependent quadrature weights given by

$$w_j = \Delta k_r \left[\frac{\sin\left(\Delta k_r\, r_j/2\right)}{\Delta k_r\, r_j/2}\right]^2. \tag{4.131}$$

Here it is interesting to note that Eq. (4.130) is identical to Eq. (4.108) except for the simple change in integration weight from Δk_r to w_j, basically applying a sinc-function squared to the field amplitude vs range. The summation can again be performed by means of an FFT or by direct summation for the ranges of interest, and is therefore insignificantly more computationally intensive that the simple FFT or trapezoidal rule integrations. The Filon quadrature scheme is obviously applicable to the integration along the complex contour as well, again involving only the change of quadrature weights to those given in Eq. (4.131).

The Filon scheme is accurate as long as the kernels are well represented by linear interpolation between the sample points. On the other hand, the error due to the nonlinear behavior of the kernel will increase with range, and the Filon scheme therefore also has a practical range limitation. Since this range limitation depends on the smoothness of the kernel, it is not possible to give any specific value. Mallick and Frazer [32] found that whereas the wavenumber sampling required for the trapezoidal rule integration is
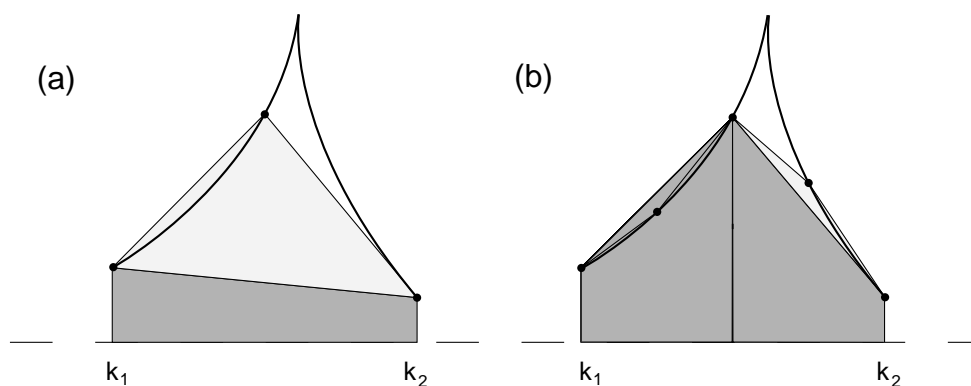
Fig. 4.12. Adaptive evaluation of wavenumber integral.

inversely proportional to ωr, the Filon scheme requires a sampling which is approximately inversely proportional to $\sqrt{\omega r}$. However, they considered seismic reflectivity problems characterized by relatively smooth wavenumber kernels. In ocean acoustics the kernel singularities are usually the controlling factor, and since the number of singularities increase with frequency, and since singularities are not necessarily better represented by a linear than a constant kernel, the improvement in computational efficiency is much less pronounced for underwater acoustic problems, and the Filon schemes are therefore rarely used.

4.5.9   Adaptive Integration

The nonlinearity of the wavenumber kernel is obviously most severe near singularities introduced by the poles and branch cuts. In other regions, e.g., in the continuous and evanescent spectra and between the modes, the kernel may be adequately represented by linear interpolation even for a relatively course sampling. Therefore, the sampling requirements are not uniform, and in some cases computational advantages can be obtained by varying the sampling along the wavenumber axis.

While the FFP integration scheme requires an equidistant sampling, the trapezoidal and Filon schemes do not have this restriction. For some problems it is known *a priori* that the integration kernel is smooth in the continuous and evanescent parts of the spectrum, and a coarse wavenumber sampling can therefore be used in these regimes, combined with a finer sampling of the discrete spectrum. However, this is not a general behavior since poles may exist in the evanescent regime for waveguides with an elastic bottom and, as illustrated by the Pekeris example, poles may even exist close to the real axis in the continuous spectrum.

These integration problems may be overcome by an adaptive selection of the wavenumber sampling. Shown in Fig. 4.12 is an example of such an adaptive scheme, developed by Krenk *et al.* [34]. Here, the kernel is first sampled on a coarse wavenumber grid, which is then subsequently subdivided by bisection, until a stable value of the integral over the sub-interval is obtained. Adaptive integration schemes involve more book-keeping in the implementation, but may improve the computational efficiency. However, for most underwater acoustic problems the computational advantages of adaptive schemes are found to be rather insignificant. Further, for computation of transmission loss, usually performed on a dense spatial grid, the fact that the adaptive sampling has to be performed individually for each receiver makes it rather intensive computationally. However, for time domain computations for a small number of receivers, it may be computationally advantageous, but since this is not the most common application of modeling in ocean acoustics, the adaptive integration techniques have never achieved the popularity they hold in crustal and exploration seismology.

4.6 Frequency Integration

The last step involved in determining the full time-domain response is the evaluation of the inverse Fourier transform,

$$g(r, z, t) = \int_{-\infty}^{\infty} g(r, z, \omega)\, e^{-i\omega t}\, d\omega \,. \tag{4.132}$$

This integral must be evaluated for all field parameters, ranges, and depths of interest. Although simple in principle, the numerical implementation of Eq. (4.132) is non-trivial. The reason is that the numerical evaluation is susceptible to the same numerical artifacts as those discussed earlier for the evaluation of the wavenumber integral. Therefore, the same issues of windowing and sampling must be properly addressed. Since the evaluation of the frequency integral is common to all numerical approaches solving the Helmholtz equation, the associated numerical issues will be deferred to Chap. 8. However, we present time-domain calculations also here (Sec. 4.8.4), due primarily to their importance in terms of interpreting the physical significance of features in the wavenumber integration kernels.

4.7 Range-Dependent Propagation

The wavenumber integration approach is applicable only to environments where the wave equation can be separated in range and depth. For a general layering of the ocean waveguide, this requires the environmental model to be horizontally stratified, with